Population spiking and bursting in next-generation neural masses with spike-frequency adaptation

Alberto Ferrara [1], David Angulo-Garcia [2], Alessandro Torcini [3,4,5] and Simona Olmi [4,5,*]

[1]*Sorbonne Université, INSERM, CNRS, Institut de la Vision, 75012 Paris, France*
[2]*Departamento de Matemáticas y Estadística, Universidad Nacional de Colombia (UNAL),
Cra 27 No. 64-60, 170003, Manizales, Colombia*
[3]*Laboratoire de Physique Théorique et Modélisation, UMR 8089, CY Cergy Paris Université, CNRS, 95302 Cergy-Pontoise, France*
[4]*CNR, Consiglio Nazionale delle Ricerche, Istituto dei Sistemi Complessi, via Madonna del Piano 10, 50019 Sesto Fiorentino, Italy*
[5]*INFN, Sezione di Firenze, via Sansone 1, 50019 Sesto Fiorentino, Italy*

Spike-frequency adaptation (SFA) is a fundamental neuronal mechanism taking into account the fatigue due to spike emissions and the consequent reduction of the firing activity. We have studied the effect of this adaptation mechanism on the macroscopic dynamics of excitatory and inhibitory networks of quadratic integrate-and-fire (QIF) neurons coupled via exponentially decaying post-synaptic potentials. In particular, we have studied the population activities by employing an exact mean-field reduction, which gives rise to next-generation neural mass models. This low-dimensional reduction allows for the derivation of bifurcation diagrams and the identification of the possible macroscopic regimes emerging both in a single and in two identically coupled neural masses. In single populations SFA favors the emergence of population bursts in excitatory networks, while it hinders tonic population spiking for inhibitory ones. The symmetric coupling of two neural masses, in absence of adaptation, leads to the emergence of macroscopic solutions with broken symmetry, namely, chimera-like solutions in the inhibitory case and antiphase population spikes in the excitatory one. The addition of SFA leads to new collective dynamical regimes exhibiting cross-frequency coupling (CFC) among the fast synaptic timescale and the slow adaptation one, ranging from antiphase slow-fast nested oscillations to symmetric and asymmetric bursting phenomena. The analysis of these CFC rhythms in the θ-γ range has revealed that a reduction of SFA leads to an increase of the θ frequency joined to a decrease of the γ one. This is analogous to what has been reported experimentally for the hippocampus and the olfactory cortex of rodents under cholinergic modulation, which is known to reduce SFA.

I. INTRODUCTION

Neural mass models are mean-field models developed to mimic the dynamics of homogenous populations of neurons. These models range from purely heuristic ones (as the well-known Wilson-Cowan model [1]), to more refined versions obtained by considering the eigenfunction expansion of the Fokker-Planck equation for the distribution of the membrane potentials [2,3]. However, quite recently, a *next-generation neural mass model* has been derived in an exact manner for heterogeneous populations of quadratic integrate-and-fire (QIF) neurons [4]. This new generation of neural mass models describes the dynamics of networks of spiking neurons in terms of macroscopic variables, like the population firing rate and the mean membrane potential, and it has already found various applications in many neuroscientific contexts [5–13].

Neural populations can display collective events, resembling spiking or bursting dynamics, observable at the single-neuron level [14,15]. In particular, in this context, tonic spiking corresponds to periodic collective oscillations (COs), while a population burst is a relaxation oscillation connecting a spiking regime to a silent (resting) state [16].

Regular collective oscillations have been reported for spiking neural populations with purely excitatory [17,18] or inhibitory interactions [19]. The emergence of these oscillations have been usually related to the presence of a synaptic timescale [20] or to a delay in the spike transmission [21]. Indeed, as shown in Refs. [7,22], the inclusion of exponentially decaying synapses in inhibitory QIF networks is sufficient for the appearance of COs, corresponding to limit cycles emerging via a Hopf bifurcation in the associated neural mass formulation.

A prominent role for the emergence of population bursts is played by spike-frequency adaptation (SFA), a mechanism for which a neuron, subject to a constant stimulation, gradually lowers its firing rate [23]. Adaptation in brain circuits is controlled by cholinergic neuromodulation. In particular an increase of the acetylcholine neuromodulator released by the cholinergic nuclei leads to a clear reduction of SFA in the Cornu Ammonis area 1 (CA1) pyramidal cells of the hippocampus [24]. Recently, it has been shown that an excitatory next-generation neural mass equipped with a mechanism of global adaptation (specifically short-term depression or SFA) can give rise to bursting behaviors [11].

*simona.olmi@fi.isc.cnr.it

Furthermore, cholinergic drugs are responsible for a modification of the neural oscillations frequency, specifically of the θ and γ rhythms [25–27], which are among the most common brain rhythms [28]. Specifically γ oscillations, which have been observed in many areas of the brain [29], have a range between $\simeq 30$ and 120 Hz, while θ oscillations correspond to 4–12 Hz in rodents [30,31] and to 1–4 Hz in humans [32]. Moreover, γ oscillations have been recently categorized in three distinct bands for the CA1 of the hippocampus [31]: a slow one ($\simeq 30$–50 Hz), a fast one ($\simeq 50$–90 Hz), and a so-termed ε band ($\simeq 90$–150 Hz). γ rhythms with similar low- and high-frequency subbands occur in many other brain regions besides the hippocampus [33,34] and they are usually modulated by slower θ rhythms in the hippocampus during locomotory actions and rapid eye movement (REM) sleep. This modulation is an example of a more general mechanism of cross-frequency coupling (CFC) between a low and a high-frequency rhythm, which is believed to be functionally relevant for the brain activity [35]: low-frequency rhythms (such as θ) usually involve broad regions of the brain and are entrained to external inputs and/or cognitive events, while high-frequency oscillations (such as γ) reflect local computation activity. Thus CFC can represent an effective mechanism to transfer information across spatial and temporal scales [35,36]. The most studied CFC mechanism is the phase-amplitude coupling, which corresponds to the modification of the amplitude (or power) of γ-waves induced by the phase of the θ oscillations; this phenomenon is often referred as θ-nested γ oscillations [37]. Cholinergic neuromodulation, and therefore SFA, has been shown to control θ-γ phase-amplitude coupling in freely moving rats in the medial entorhinal cortex [38] and in the prefrontal cortex [39].

In this paper we want to compare the role played by the spike-frequency adaptation in shaping the emergent dynamics in two simple setups: either purely inhibitory or purely excitatory neural networks. In this regard we consider fully coupled QIF neurons with SFA, interacting via exponentially decaying post-synaptic potentials. The spike-frequency adaptation is included in the model via an additional collective afterhyperpolarization (AHP) current, which temporarily hyperpolarizes the cell upon spike emission, with a recovery time of the order of hundreds of milliseconds [23,25,40]. We will first analyze the dynamics of an isolated population with SFA and then extend the analysis to two symmetrically coupled populations. In the latter case we will focus on the emergence of collective solutions (either asynchronous or characterized by population spiking and bursting) with particular emphasis of the symmetric or nonsymmetric nature of the dynamics displayed by each population [41].

The emergence of CFC among oscillations in the θ and γ range have been previously reported for next-generation neural masses: namely, for two asymmetrically coupled inhibitory populations with different synaptic timescales [7], as well as for inhibitory and excitatory-inhibitory networks under an external θ-drive [10]. Here, we show that, in presence of SFA, θ-γ CFCs naturally emerge in absence of external forcing and for symmetrically coupled populations. The cross-frequency coupling is due to the presence of a fast timescale associated to the synaptic dynamics and a slow one relative to the

adaptation. Quite peculiarly, inhibitory interactions give rise to slow γ oscillations (30–60 Hz), while excitatory ones are associated to fast γ rhythms (60–130 Hz). Furthermore, we will show that SFA controls the frequency of the slow and fast rhythms as well as the entrainement among θ and γ rhythms.

This paper is organised as follows. Section II is devoted to the introduction of the QIF neuron and of the studied network models, as well as to the presentation of the corresponding neural mass models. The methods employed to characterize the linear stability of the stationary solutions for a single and two coupled populations are reported in Sec. II D. In Sec. III A the regions of existence of population spikes and bursts are identified for a single population with SFA together with the bifurcation diagrams displaying the possible collective dynamical regimes. The analysis is then extended to two symmetrically coupled excitatory or inhibitory populations without SFA in Sec. III B and with SFA in Sec. III C. The relevance and influence of SFA for θ-γ CFC for two symmetrically coupled populations is examined in Sec. IV. Finally a summary and a brief discussion of the results is reported in Sec. V. The Appendix summarizes the methods employed to study the linear stability of the stationary solutions for a single population.

II. MODEL AND METHODS

A. Quadratic integrate and fire (QIF) neuron

As single-neuron model we consider the QIF neuron, which represents the normal form of Hodgkin class I excitable membranes [42] and it allows for exact analytic treatments of network dynamics at the mean-field level [4]. The membrane potential dynamical evolution for an isolated QIF neuron is given by

$$\tau \dot{V}(t) = V^2(t) + \eta, \tag{1}$$

where $\tau = 10$ ms is the membrane time constant and η is the excitability of the neuron.

The QIF neuron exhibits two possible dynamics depending on the sign of η. For negative η the neuron is excitable, and for any initial condition $V(0) < \sqrt{-\eta}$ it reaches asymptotically the resting value $-\sqrt{-\eta}$. However, for initial values larger than the excitability threshold, $V(0) > \sqrt{-\eta}$, the membrane potential grows unbounded and a reset mechanism has to be introduced together with a formal spike emission to mimic the spiking behavior of a neuron. As a matter of fact, whenever $V(t)$ reaches a threshold value V_{th}, the neuron delivers a formal spike and its membrane voltage is reset to V_r; for the QIF neuron $V_{th} = -V_r = \infty$. In other words the QIF neuron emits a spike at time t_k whenever $V(t_k^-) \to \infty$, and it is instantaneously reset to $V(t_k^+) \to -\infty$. For positive η, the neuron is suprathreshold and it delivers a regular train of spikes with frequency $\sqrt{\eta}/\pi$.

B. Network models of QIF neurons

We consider a heterogeneous network of N fully coupled QIF neurons with spike-frequency adaptation (SFA). The

membrane potential dynamics of QIF neurons can be written as

$$\tau \dot{V}_i(t) = V_i^2(t) + \eta_i + JS(t) - A_i(t), \quad (2a)$$

$$\tau_A \dot{A}_i(t) = -A_i(t) + \alpha \sum_{m|t_m^i < t} \delta(t - t_m^i) \quad (2b)$$

$$i = 1, \ldots, N,$$

$$\tau_S \dot{S}(t) = -S(t) + \frac{1}{N} \sum_{j=1}^{N} \sum_{k|t_k^j < t} \delta(t - t_k^j), \quad (2c)$$

where the network dynamics is given by the evolution of $2N + 1$ degrees of freedom. Here, η_i is the excitability of the ith neuron and J is the synaptic strength which is assumed to be identical for each synapse. The sign of J determines if the presynaptic neuron is excitatory ($J > 0$) or inhibitory ($J < 0$). Moreover, $S(t)$ is the global synaptic current accounting for all the previously emitted spikes in the network, where $t_k^j < t$ is the spike time emission of the kth spike delivered by neuron j. We assumed exponentially decaying PSPs with decay rate τ_S, therefore $S(t)$ is simply the linear superposition of all the PSPs emitted at previous times in the whole network. Since we have considered a fully coupled network, $S(t)$ is the same for each neuron. The adaptation variable $A_i(t)$ accounts for the decrease in the excitability due to the activity of neuron i. Each time the neuron emits a spike at time t_k^i, the variable A_i is increased by a quantity α and the effect of the spikes is forgotten exponentially with a decay constant τ_A. We termed this version of the network model μ-SFA, since it accounts for the adaptability at a microscopic level.

However, as shown in Ref. [9], by assuming that the spike trains received by each neuron have the same statistical properties of the spike train emitted by a single neuron (apart from obvious rescaling related to the size), the SFA can be included in the model also in a mesoscopic way. In this case the evolution equations for the membrane potentials read as

$$\tau \dot{V}_i(t) = V_i^2(t) + \eta_i + JS(t) - A(t), \quad (3a)$$

$$i = 1, \ldots, N,$$

$$\tau_A \dot{A}(t) = -A(t) + \frac{\alpha}{N} \sum_{j=1}^{N} \sum_{k|t_k^j < t} \delta(t - t_k^j), \quad (3b)$$

$$\tau_S \dot{S}(t) = -S(t) + \frac{1}{N} \sum_{j=1}^{N} \sum_{k|t_k^j < t} \delta(t - t_k^j), \quad (3c)$$

where the number of ODEs describing the network dynamics is now reduced to $N + 2$ and the SFA dynamics is common to all neurons and driven by the population firing rate

$$r(t) = \frac{1}{N} \sum_{j=1}^{N} \sum_{k|t_k^j < t} \delta(t - t_k^j). \quad (4)$$

In the following we will denote this network model as m-SFA. The treatment of the N adaptability variables $\{A_i\}$ in terms of a single mesoscopic one is clearly justified (i) for relatively narrow distributions of the excitabilities with respect to the median excitability value [13,43] and (ii) for sufficiently long

adaptive timescale $\tau_A \gg \tau_S$. While the former assumption implies limiting the variability of the firing rates of the single neurons, the latter allows us to neglect the modulations of the firing rates on synaptic timescales [11].

In a large part of the paper, we will consider adimensional time units, therefore the variables entering in Eqs. (2) and (3) will be rescaled as follows:

$$\tilde{t} = \frac{t}{\tau} \quad \tilde{S} = \tau S, \quad \tilde{A}_i = \tau A_i, \quad \tilde{A} = \tau A, \quad (5)$$

and the timescales as

$$\tau_s = \frac{\tau_S}{\tau}, \quad \tau_a = \frac{\tau_A}{\tau}. \quad (6)$$

Only in the final Secs. IV and V, we will come back to dimensional time units to make easier the comparison with experimental findings. To simplify the notation and without lack of clarity we will omit in the (˜) symbol on the adimensional variables and parameters.

C. Neural mass models

1. Single neural population

As shown in Ref. [4], a neural mass model describing the macroscopic evolution of a fully coupled heterogeneous QIF spiking network with instantaneous synapses can be derived analytically, by assuming that the excitabilities $\{\eta_i\}$ follow a Lorentzian distribution

$$g(\eta) = \frac{1}{\pi} \frac{\Delta}{(\eta - \bar{\eta})^2 + \Delta^2}, \quad (7)$$

where $\bar{\eta}$ is the median value of the distribution and Δ is the half-width at half-maximum (HWHM), accounting for the dispersion of the distribution. The derivation is possible for the QIF neuronal model, since its dynamical evolution can be rewritten in terms of purely sinusoidal functions of a phase variable. This allows us to apply the Ott-Antonsen Ansatz, introduced for phase oscillator networks [44], in the context of spiking neural networks [45,46]. In particular, the analytic derivation reported in Ref. [4] allows us to rewrite the network dynamics in terms of only two collective variables: the population firing rate $r(t)$ and the mean membrane potential $v(t) = \sum_{i=1}^{N} V_i(t)/N$. The neural mass thus introduced can be extended to include finite synaptic decays; for exponentially decaying synapses it takes the following form [22]:

$$\dot{r} = \frac{\Delta}{\pi} + 2rv, \quad (8a)$$

$$\dot{v} = v^2 + \bar{\eta} - (\pi r)^2 + Js, \quad (8b)$$

$$\tau_s \dot{s} = -s + r, \quad (8c)$$

where a third variable in now present, $s(t)$, representing the global synaptic field.

The inclusion of SFA in the neural mass model Eqs. (8) is straightforward when considering the m-SFA, since, in this context, the adaptability is described by a collective variable. This finally leads to the following four dimensional mesoscopic model for a single QIF population,

$$\dot{r} = \frac{\Delta}{\pi} + 2rv, \quad (9a)$$

$$\dot{v} = v^2 + \bar{\eta} - (\pi r)^2 + Js - A, \quad (9b)$$

$$\tau_s \dot{s} = -s + r, \tag{9c}$$

$$\tau_a \dot{A} = -A + \alpha r, \tag{9d}$$

which represents the exact mean-field formulation of the QIF spiking network with m-SFA, described by the $N + 2$ set of ODEs (3), in the limit $N \to \infty$. However, as we will show thereafter, it can also capture the dynamics of the network with μ-SFA, described by the set of ODEs (2) and characterized by $N^2 + 1$ variables, for limited neural heterogeneity (i.e., sufficiently small Δ) and sufficiently long adaptive timescales τ_a.

2. Two symmetrically coupled neural population

The dynamics of two symmetrically coupled identical neural masses with adaptation is described by the 8-dim system of ODEs,

$$\dot{r}_{1,2} = \frac{\Delta}{\pi} + 2r_{1,2}v_{1,2}, \tag{10a}$$

$$\dot{v}_{1,2} = v_{1,2}^2 + \bar{\eta} - (\pi r_{1,2})^2 + J_s s_{1,2} + J_c s_{2,1} - A_{1,2}, \tag{10b}$$

$$\tau_s \dot{s}_{1,2} = -s_{1,2} + r_{1,2}, \tag{10c}$$

$$\tau_a \dot{A}_{1,2} = -A_{1,2} + \alpha r_{1,2}, \tag{10d}$$

where J_s and J_c represent the self- and cross-coupling, respectively.

On the basis of Eqs. (10), one cannot distinguish between the two populations, therefore these equations are invariant under the permutation of the variables $(r_1, v_1, s_1, A_1, r_2, v_2, s_2, A_2) \longrightarrow (r_2, v_2, s_2, A_2, r_1, v_1, s_1, A_1)$ and they admit the existence of entirely symmetric solutions $(r_1, v_1, s_1, A_1) \equiv (r_2, v_2, s_2, A_2)$.

By following Ref. [41], we analyze the stability of symmetric solutions by transforming the original set of variables in the following ones:

$$\begin{pmatrix} r_{l,t} \\ v_{l,t} \\ s_{l,t} \\ A_{l,t} \end{pmatrix} = \frac{1}{2} \left\{ \begin{pmatrix} r_2 \\ v_2 \\ s_2 \\ A_2 \end{pmatrix} \pm \begin{pmatrix} r_1 \\ v_1 \\ s_1 \\ A_1 \end{pmatrix} \right\}, \tag{11}$$

where we refer to (r_l, v_l, s_l, A_l) and (r_t, v_t, s_t, A_t) as the longitudinal and transverse set of coordinates, respectively.

In this new set of coordinates, the trajectories of the symmetric solutions live in the invariant subspace $(r_l, v_l, s_l, A_l, r_t \equiv 0, v_t \equiv 0, s_t \equiv 0, A_t \equiv 0)$, with the longitudinal variables satisfying the following set of ODEs:

$$\dot{r}_l = \frac{\Delta}{\pi} + 2r_l v_l, \tag{12a}$$

$$\dot{v}_l = v_l^2 + 1 - (\pi r_l)^2 + (J_s + J_c)s_l - A_l, \tag{12b}$$

$$\tau_s \dot{s}_l = s_l - r_l, \tag{12c}$$

$$\tau_a \dot{A}_l = A_l - \alpha r_l. \tag{12d}$$

D. Linear stability analysis

1. Stationary solutions for a single population

By following Ref. [22], we explore the stability of the stationary solutions of the single QIF population, corresponding to fixed-point solutions (r_0, v_0, s_0, A_0) in the neural mass for-

mulation (9). These fixed-point solutions are given by $s_0 = r_0$, $A_0 = \alpha r_0$, together with the implicit algebraic system

$$v_0 = -\frac{\Delta}{2\pi r_0}, \tag{13}$$

$$0 = v_0^2 + \bar{\eta} + J r_0 - \pi^2 r_0^2 - \alpha r_0. \tag{14}$$

Notice that the whole equilibrium solution can be parametrized in terms of r_0.

The linear stability analysis of the fixed point can be performed by estimating the eigenvalues λ of the associated Jacobian matrix

$$\mathbf{H} = \begin{pmatrix} 2v_0 & 2r_0 & 0 & 0 \\ -2\pi^2 r_0 & 2v_0 & J & -1 \\ \frac{1}{\tau_s} & 0 & -\frac{1}{\tau_s} & 0 \\ \frac{\alpha}{\tau_a} & 0 & 0 & -\frac{1}{\tau_a} \end{pmatrix}. \tag{15}$$

The eigenvalues are the solutions of the corresponding characteristic polynomial $p(\lambda)$. In particular, assuming $\lambda = i\Omega$ leads to the Hopf bifurcation curves, while setting $\lambda = 0$ leads to saddle-node and pitchfork bifurcations. This analysis is performed in details in the Appendix.

2. Stationary solutions for two coupled populations

The stability of the symmetric solutions of Eqs. (12) can be examined in the longitudinal or transverse manifold by employing the transformation of variables reported in Eq. (11). In particular, as seen in many contexts ranging from chaotic maps [47] to chimera states [48], the longitudinal instabilities preserve the symmetric nature of the solutions, while the transverse ones are responsible for symmetry breaking.

Here, we will focus on the linear stability of symmetric stationary solutions, corresponding to fixed points $(\bar{r}_l, \bar{v}_l, \bar{s}_l, \bar{A}_l)$ of Eqs. (12). The linear and transverse stability analysis can be performed by considering the linearized evolution around the fixed points given by

$$\begin{pmatrix} \delta \dot{r}_{l,t} \\ \delta \dot{v}_{l,t} \\ \delta \dot{s}_{l,t} \\ \delta \dot{A}_{l,t} \end{pmatrix} = \mathbf{H}_{l,t} \begin{pmatrix} \delta r_{l,t} \\ \delta v_{l,t} \\ \delta s_{l,t} \\ \delta A_{l,t} \end{pmatrix}, \tag{16}$$

with

$$\mathbf{H}_{l,t} = \begin{pmatrix} 2\tilde{v}_{l,t} & 2\tilde{r}_{l,t} & 0 & 0 \\ -2\pi^2 \tilde{r}_{l,t} & 2\tilde{v}_{l,t} & J_s \pm J_c & -\frac{1}{\tau_a} \\ \frac{1}{\tau_s} & 0 & -\frac{1}{\tau_s} & 0 \\ \frac{\alpha}{\tau_a} & 0 & 0 & -\frac{1}{\tau_a} \end{pmatrix}. \tag{17}$$

The longitudinal and transverse stability of the fixed points can be analysed by considering the eigenvalue problems associated to $\mathbf{H}_l$ and $\mathbf{H}_t$, respectively. In particular, we notice that the stability can be lost in two different ways: (i) one eigenvalue becomes exactly equal to 0 (similarly to a limit point); (ii) the real part of two complex conjugates eigenvalues becomes exactly zero (Hopf bifurcation).

Therefore, we have a total of four possible changes of stability of the symmetric stationary solutions giving rise to

the following bifurcations in the complete eight-dimensional phase space:

(1) *Longitudinal limit point bifurcation (LLP):* Saddle-node bifurcation in the original system;

(2) *Longitudinal Hopf bifurcation (LH):* Hopf bifurcation generating symmetric oscillations;

(3) *Transverse limit point bifurcation (TLP):* Branch-point or pitchfork bifurcation in the original system giving rise to two different equilibria for the two populations;

(4) *Transverse Hopf bifurcation (TH):* Hopf bifurcation in the original system generating asymmetric oscillations for the two populations, which can differ simply in their phase or even in amplitude and phase.

The transverse and longitudinal stability analysis of the symmetric solutions is verified and complemented by employing standard continuation packages (such as MATCONT [49]) over the dynamics of the complete system (10),

III. RESULTS

The analysis reported in this paper will be focused on neural mass models, however, before reporting the corresponding results, let us compare in a few cases the simulations done separately for the network and the neural masses. As previously stated, the neural mass model (8) reproduces exactly the population dynamics of a network of QIF spiking neurons with m-SFA (3) for a sufficiently large number of neurons. Indeed, as shown in Fig. 1, the agreement between the neural mass (red solid line) and the network simulations (blue squares) is very good already for $N > 10\,000$ for different macroscopic regimes observable in purely inhibitory or excitatory populations. For what concerns the μ-SFA network model (2) (black circles), while in the asynchronous regime (stationary state) the agreement with the other two models is noticeable [see Fig. 1(a)], in presence of collective oscillations there is a clear dephasing between neural mass and μ-SFA dynamics at sufficiently long times [see Figs. 1(b) and 1(c)]. In general, the μ-SFA networks will display the same macroscopic states and bifurcation structure as the neural mass models. However, discrepancies among the two approaches should be expected for low median excitability with a high level of heterogeneity or for faster adaptation timescales, as shown in Refs. [11,13,43].

A. Single population with SFA

In this subsection we analyze the relevance of SFA for the emergence of collective dynamics. In particular, we consider a single heterogeneous population of QIF neurons with SFA. All the results here reported are based on the linear stability analysis of the stationary solutions of the neural mass models, as discussed in Sec. II D 1 and the Appendix.

In the absence of adaptation, the excitatory population with exponentially decaying synapses displays only fixed-point solutions (namely, foci): for sufficiently negative (positive) $\bar{\eta}$, a single stable fixed point is present corresponding to a low (high) firing rate solution, while just below $\bar{\eta} = 0$, the two solutions coexist. For exponentially decaying synapses both fixed points are foci, characterized by one real and two complex conjugate eigenvalues, at variance with what reported in the absence of a synaptic timescale [4], where the low firing
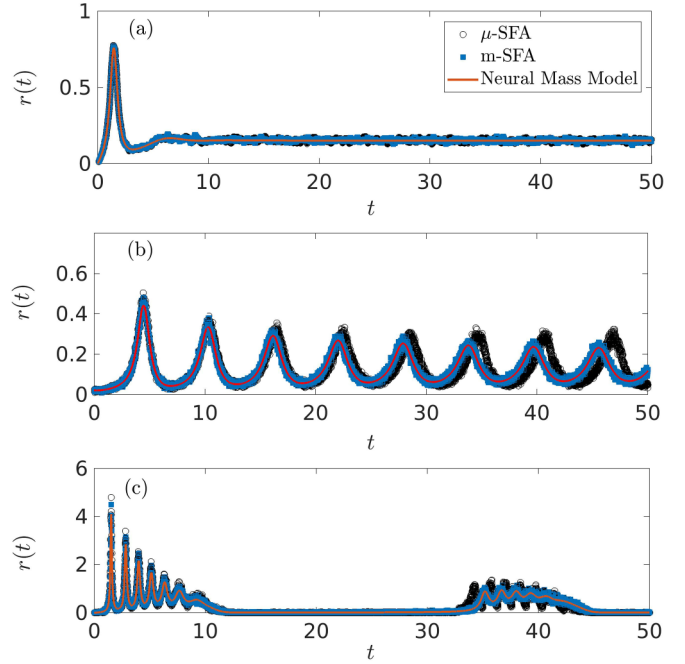

FIG. 1. Comparison of population firing rate $r(t)$ as obtained by the network models with μ-SFA (2) (black circles) and with m-SFA (3) (blue squares), with the evolution of the neural mass models (8) (red line) for different macroscopic behaviors: (a) stationary state (parameters $J = -6$, $\Delta = 0.5$, $\alpha = 1$); (b) population spiking ($J = -6$, $\Delta = 0.12$, $\alpha = 1$); and (c) population bursting ($J = 15$, $\Delta = 0.12$, $\alpha = 20$). Other parameters are $\tau_s = 1.5$, $\tau_a = 10$, and $\bar{\eta} = 1$. For the network simulations the number of considered QIF neurons is $N = 10\,0000$ [panel (a)] or $N = 100\,000$ [panels (b) and (c)]. For all comparisons the neural mass model has been integrated starting from initial values of r, v, A, and s as obtained from the microscopic state of the considered networks.

solution is a node, not a focus. However, in the inhibitory case, one observes tonic population spiking in a limited range of synaptic timescales $\tau_s \simeq 0.1$–100 and for not too wide heterogeneity distributions and synaptic coupling strenghts $|J|$ [7,22]. In this case the period of the COs is essentially controlled by the synaptic timescale, since the oscillations emerge due to the inhibitory action that desynchronizes the spiking activity [22].

In the presence of SFA, COs are observable both in purely excitatory and inhibitory populations, as shown in Fig. 2(a), where the Hopf bifurcation lines are reported (as solid lines) in the $(J, \bar{\eta})$ plane at different values of the HWHM of the heterogeneity Δ. In the inhibitory case, for the present choice of synaptic and adaptation timescales, COs emerge for any value of $|J|$, for sufficiently large excitatory drive $\bar{\eta}$, i.e., above the Hopf bifurcation curves shown in Fig. 2(a) for $J < 0$. For increasing Δ, the Hopf curve moves at higher values of $\bar{\eta}$, thus indicating that a higher excitatory drive is required to overcome the heterogeneity present in the population. In the excitatory case, stable COs are instead limited to a small portion of the plane in proximity of $\bar{\eta} \approx 0$ and $J \simeq 5$–10, as shown the inset of Fig. 2(a). The COs are stable within the closed loop in the $(J, \bar{\eta})$ plane, while, outside the loop, the macroscopic limit cycles are unstable and eventually both
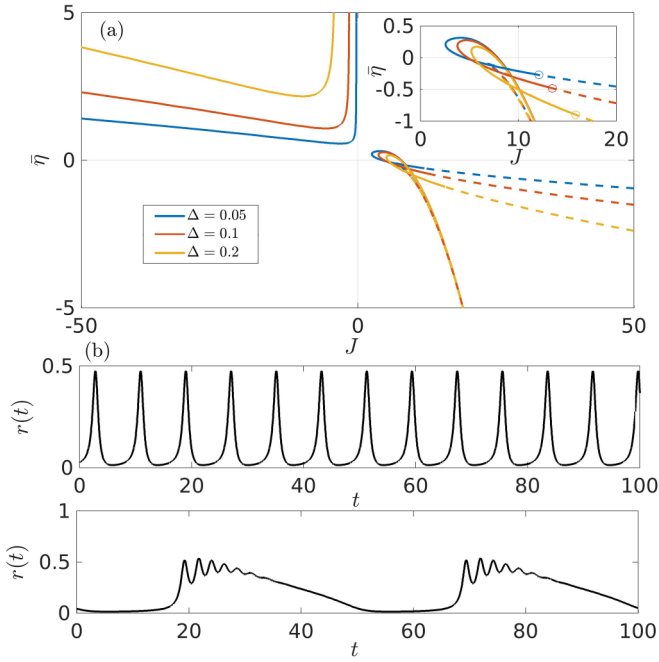
FIG. 2. Single neural mass with SFA. (a) Hopf boundaries in the $(J, \bar{\eta})$ space at different values of Δ. Parameters used here $\tau_s = 2$, $\tau_a = 10$, and $\alpha = 5$. Solid lines refer to Hopf curves while dashed lines refer to saddle-node curves. At $J > 0$ the Hopf curves meet with the saddle node curves at Bogdanov Takens points (circle), as shown in the inset. (b) Oscillations generated within the Hopf region in the inhibitory case with $\eta = 1$ and $J = -7$ (top) and the excitatory case with $\eta = 0.1$ and $J = 7$ (bottom). In both cases $\Delta = 0.05$ was used.

FIG. 3. Single neural mass with SFA. The population firing rate r versus $\bar{\eta} - A$ for the population burst solution displayed in Fig. 2(b) (bottom). The solid (dashed) black lines refer to stable (unstable) fixed points of the fast subsystem [Eqs. (9a)–(9c)]. The filled black squares denote the saddle-node bifurcations in the fast subsystem. The red solid line is the bursting solution of the complete system (9), where the black arrows indicate the time evolution along such a solution. In the upper insets are shown the population firing rate $r(t)$ and the adaptation variable $A(t)$ as a function of time during the evolution of the population burst. Parameters as described in the caption of Fig. 2.

branches of the Hopf curve end at a Bogdanov Takens (BT) bifurcation point of codimension two (circles in the inset) [50]. As expected, at this point, saddle-node bifurcation curves of fixed points (dashed lines) emerge.

As it can be seen in Fig. 2(b), COs generated via inhibition (top) are population spikes characterized by an unique oscillation period, whose value is controlled by α and which can range form τ_s to τ_a. However, excitatory mediated COs (bottom) are characterized by two frequencies: a slow one (definitely longer than τ_a), responsible for the alternation of silence and high activity in the population and a fast one (of the order of τ_s), controlling the fast damped oscillations developing on top of the slow carrier. These kind of COs have been termed emergent bursting or population bursting, in analogy with the bursting activity of the single neurons [11,51]. To better understand the origin of these population bursts we have performed a standard slow-fast analysis, by considering as fast subsystem the one with constant adaptation A. In particular, we analyze the possible solutions emerging in the fast subsystem [Eqs. (9a)–(9c)] as a function of the control parameter $\bar{\eta} - A$. The solutions are stable (unstable) fixed points reported as solid (dashed) black lines in Fig. 3 and they correspond to a low and a high firing solution that can coexist in a certain interval of the parameter values $\bar{\eta} - A$. Together with the fast subsystem solutions, we display also the population burst (solid red line) obtained for the full equation system (9) as $r(t) = r[\bar{\eta} - A(t)]$. As shown in the upper insets of
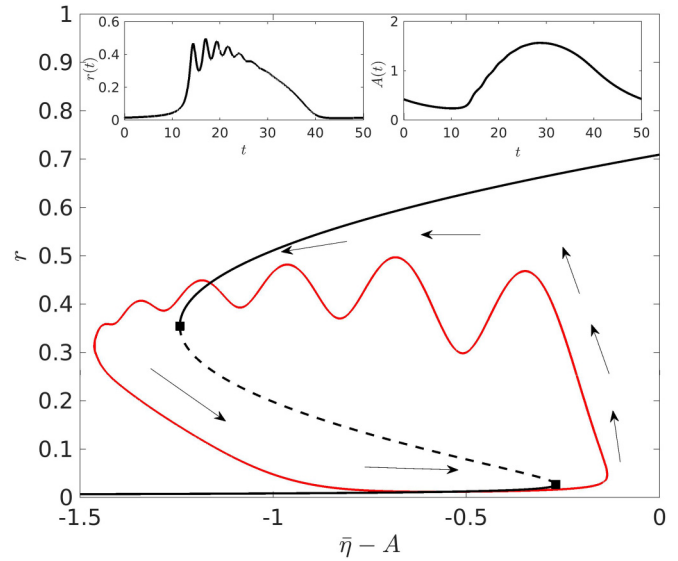
Fig. 3, the variable $A(t)$ displays regular periodic oscillations with period τ_a, each complete oscillation corresponding to a population burst in the variable $r(t)$.

By examining the evolution of the bursting solution in Fig. 3, we observe that the orbit is initially lying on the lower stable solution branch of the fast subsystem. However, during the burst evolution (indicated by the black arrows) the variable $A(t)$ decreases. This decrease finally leads the orbit beyond the region of existence of the lower branch, where only the higher branch state is present and stable. Afterwards, the orbit is attracted towards the focus in the upper branch and approaches it by displaying damped oscillations with periods of the order of $\simeq 1.1$–2.8. In the meantime, the variable A is growing. The growth of A leads the burst orbit beyond the region of existence of the upper state and, consequently, the orbit is attracted back towards the only stable solution, i.e., the lower state, and the orbit evolution repeats. However, it still remains an aspect to be clarified regarding this slow-fast analysis: why the orbit approaches the upper state by displaying damped oscillations, while it approaches the lower state without such oscillations, despite both solutions are foci of the fast subsystem. This is due to the fact that the period of the damped oscillations in the lower branch is definitely larger than the characteristic period of the population bursts t_a (namely, $\simeq 12$–40), and therefore oscillations cannot be observed on this timescale.

The effect of the adaptation on the population dynamics can be better appreciated by considering the bifurcation diagram in the (J, α) plane for different Δ values, as shown in
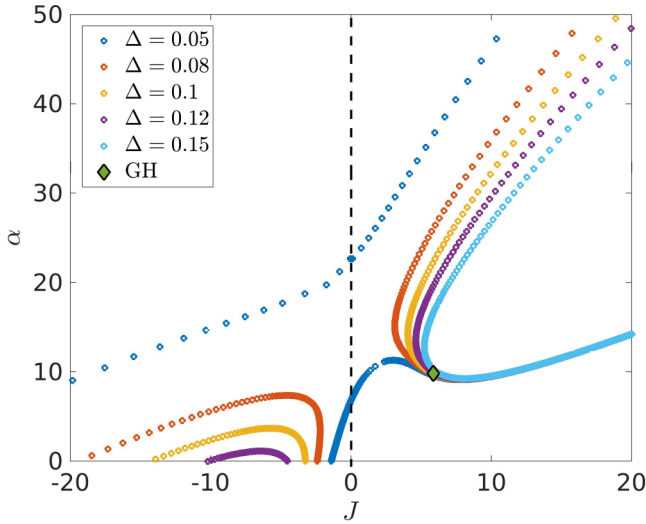
FIG. 4. Single neural mass with SFA. Hopf boundaries in the (J, α) space at different values of Δ. Parameters used here: $\tau_s = 2$, $\tau_a = 10$, and $\bar{\eta} = 1$. Dashed vertical line separates the excitatory regime from the inhibitory one. The symbol refers to the generalized Hopf (GH) bifurcation point for $\Delta = 0.1$ located at $(J, \alpha) = (5.86, 9.81)$.

Fig. 4. As already mentioned, in the excitatory case no COs are observable in the system in the absence of adaptation. Instead, in the presence of SFA there is a wide region where population bursts can be observed for sufficiently large α and for any Δ: the region inside each Hopf bifurcation curve, identified by circles of different colors for each Δ value in Fig. 4. In this case, on the lower Hopf bifurcation curve, a generalized Hopf (GH) point is observable, distinguishing supercritical (at smaller J) from subcritical Hopf-bifurcations (at larger J); an example is shown for $\Delta = 0.1$ in Fig. 4. Just above the subcritical line one has a region where population bursts and stationary foci coexist, similarly to what is reported in Ref. [11] for an adaptation current with an α-kernel and instantaneous synapses.

For the inhibitory case an interval of synaptic strength J where COs are present can be identified even at $\alpha = 0$, for sufficiently small $\Delta \lesssim 0.13$: it is the interval between the crossing of the Hopf curves with the zero axis in Fig. 4. The presence of adaptation shrinks the interval where COs can be observed, having in this case an opposite effect with respect to what seen for an excitatory population. This is true for sufficiently large heterogeneity $\Delta > \Delta_c \simeq 0.063271$, while, below the critical value Δ_c, the Hopf curves for excitatory and inhibitory populations merge together, giving rise to a wide region where COs are observable (see the blue circles in Fig. 4 delimiting the internal region of existence of COs for $\Delta = 0.05$).

In summary, the adaptation has a twofold effect of promoting COs in excitatory neural masses and preventing their emergence in inhibitory ones. This can be explained by the fact that in the excitatory case the only source of inhibition arises from SFA. As a consequence, we can expect that the adaptation timescale plays a role somehow similar to that of the synaptic timescale in purely inhibitory networks for

the emergence of COs [19]. In the inhibitory case the effect of adaptation is to increase the inhibitory effect and to slow down the inhibitory response, thus, for sufficiently large α, the COs can eventually disappear for a mechanism similar to that reported in Refs. [7,22] in the absence of adaptation.

B. Two coupled populations without SFA

In this subsection we analyze the dynamical regimes emerging in two symmetrically coupled neural mass models without adaptation, corresponding to Eqs. (10) with $\alpha = 0$. In particular, we vary the cross-coupling and the median excitability as control parameters, thus evaluating the bifurcation diagram in the bidimensional plane $(J_c, \bar{\eta})$. The synaptic timescale τ_s, the level of heterogeneity Δ and the self-coupling J_s are kept fixed.

1. Two inhibitory populations

Let us first consider two inhibitory neural masses that display, when uncoupled, a stationary solution (fixed point) for sufficiently small $\bar{\eta} < \eta_c$, and COs for larger $\bar{\eta} > \eta_c$. Once symmetrically coupled, the two populations can display various dynamical regimes emerging from the stable fixed points due to longitudinal or transverse instabilities, as shown in Fig. 5. In the present analysis as well as in the following, we will only consider transitions associated to stable states (solid lines in Fig. 5) and we will neglect those corresponding to unstable states (dashed lines).

In particular, the longitudinal Hopf (LH) instability [blue solid line in Fig. 5(a)] divides the plane $(J_c, \bar{\eta})$ in two parts: one associated to fixed points (COs) below (above) the line. The LH line is the continuation of the critical point η_c, found at $J_c \equiv 0$, to finite cross-couplings. Another bifurcation curve corresponding to a transverse instability is reported in Fig. 5(a). This is a TLP bifurcation line (red solid curve): the dynamical evolution of the two populations is identical (different) to the right (to the left) of this curve. The LH and TLP bifurcation lines meet at a zero-Hopf (ZH) point, thus creating 4 different regions with distinct types of dynamics. For each region the evolution of the firing rate of population 1 (population 2) is shown in Figs. 5(b)–5(e) as blue (red) solid line, and they correspond to the following regimes:

(1) region I: the two firing rates are constant and identical [see Fig. 5(b)];

(2) region II: the two firing rates are constant but with different values [see Fig. 5(c)];

(3) region III: the two firing rates oscillate in perfect synchrony [see Fig. 5(d)];

(4) region IV: the two firing rates oscillates with different amplitudes, the two populations oscillate in phase but their activity is different [see Fig. 5(e)].

The collective periodic oscillations here reported can be all identified as population spikes [14], where a large part of the neurons fires within a short time window and their periods are obviously related to the synaptic timescale τ_s [22].

The nonidentical solutions observable in Figs. 5(c) and 5(e) correspond to a spontaneous symmetry breaking of the dynamical evolution and they emerge for $|J_c| > |J_s|$. In particular, these solutions can be identified as generalized chimera states [41,52], where the two populations display different
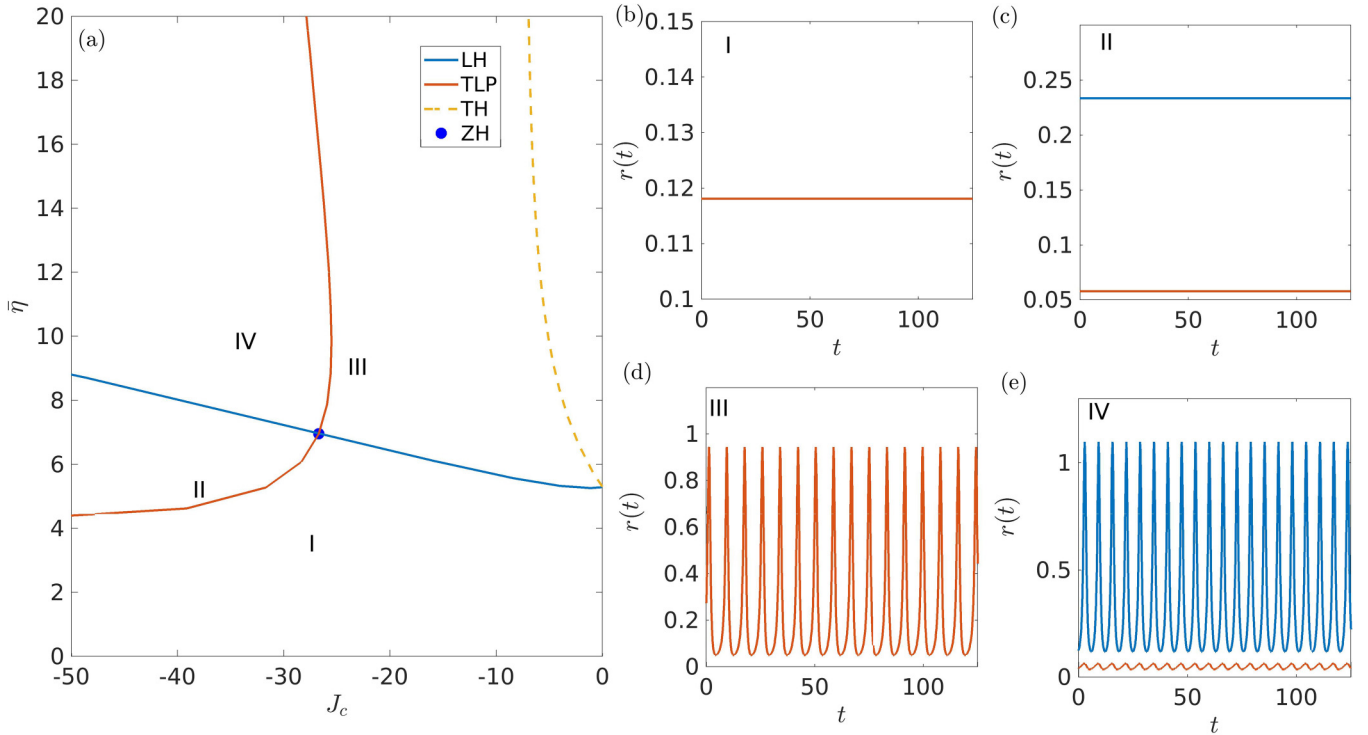
FIG. 5. Two symmetrically coupled inhibitory populations without adaptation. (a) Phase diagram in the $(J_c, \bar{\eta})$ space showing the longitudinal (blue solid line) and transverse (red solid line) stability boundaries. Stability boundaries of stable (unstable) solutions are shown as (solid) dashed lines. Longitudinal and transverse stability boundaries meet at a zero-Hopf point dividing the parameter space in four regions. A sample time trace of the firing rate of each population is shown in panels (b)–(e) for the four possible dynamical regimes: (b) region I, symmetric fixed points $(J_c, \bar{\eta}) = (-25, 5)$; (c) region II, asymmetric fixed points $(J_c, \bar{\eta}) = (-33, 7)$; (d) region III, symmetric COs $(J_c, \bar{\eta}) = (-25, 10)$; (e) region IV, asymmetric COs $(J_c, \bar{\eta}) = (-33, 10)$. The blue (red) solid lines in panels (b)–(e) denotes the firing rate of population 1 (population 2). Other parameters for this figure: $\tau_s = 2$, $\Delta = 0.5$, $J_s = -20$, and $\alpha = 0$.

levels of synchronization characterized by constant [as in Fig. 5(c)] or periodically [as in Fig. 5(e)] oscillating Kuramoto order parameters [53], as we have verified by employing the conformal transformation introduced in Ref. [4], which relates the Kuramoto order parameter to the mean membrane potential and the population firing rate.

2. Two excitatory populations

As a complementary analysis, we consider now two identically coupled excitatory neural masses. In this case, for sufficiently low values of the cross-coupling J_c, we observe two coexisting symmetric fixed points, corresponding to a low and a high-activity state of the neural population, analogously to what found for a single population. These solutions are shown in Fig. 6(a) as a function of $\bar{\eta}$ for increasing values of J_c. At low values (namely, $J_c = 10$ and 20) we observe that the low-activity state looses its stability by increasing $\bar{\eta}$ via a saddle-node bifurcation; this fixed point is connected to the high-activity state via an unstable solution that turns to be stable via a second saddle-node bifurcation. In particular, we observe a coexistence region between the two solutions delimited by the occurrence of the two saddle-node bifurcations. At larger cross-coupling ($J_c = 40$) the high-activity state is instead always unstable.

The complete scenario can be better understood by considering the two dimensional phase diagram in the plane

$(J_c, \bar{\eta})$, shown in Fig. 6(b), obtained by computing longitudinal and transverse instabilities for this system. Let us first focus on the part of phase diagram delimited by the vertical line $J_c \lesssim 32.5$ (yellow solid line) where one has only symmetric solutions and three distinct regions separated by two longitudinal saddle-node bifurcation curves (LLP) are observables:

(1) region I: a unique stable low-activity fixed point corresponding to the lower branch of equilibria in Fig. 6(a);

(2) region II: coexistence of two fixed points corresponding to high and low activity. The region inside the red dashed curve corresponding to a TLP bifurcation line is not observable, since it is related to the continuation of the branch point appearing in the unstable branch in Fig. 6(a) at low J_c;

(3) region III: an unique stable high-activity fixed point corresponding to the stable upper branch of equilibria in Fig. 6(a).

At $J_c \approx 32.5$ a spontaneous symmetry breaking occurs in the system, due to a transverse Hopf instability (TH), leading to the emergence of collective antiphase oscillations from the high-activity fixed point. These COs are characterized by extremely fast periods of oscillation definitely smaller than the synaptic time constant τ. Here two other dynamical regimes are now observable:

(1) region IV: the stable high-activity point is no longer stable, and an asymmetric solution where both populations oscillate in antiphase appears;
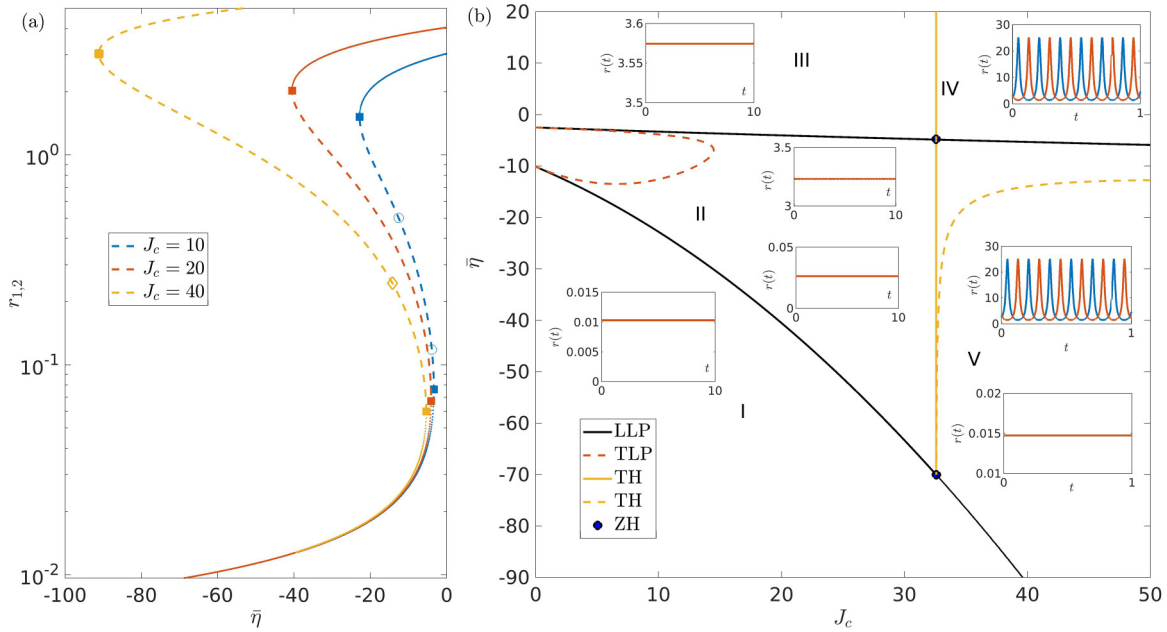
FIG. 6. Two symmetrically coupled excitatory populations without adaptation. (a) Evolution of the population firing rates $r_{1,2}$ versus $\bar{\eta}$ for the stationary solution corresponding to an asynchronous regime. The fixed-point solutions are shown for three different values of the cross-coupling: namely, $J_c = 10$ (blue lines), 20 (red lines), and 40 (yellow lines). Stable (unstable) solutions are denoted by solid (dashed) lines, saddle-node bifurcations ae denoted by filled squares, pitchfork bifurcations by empty circles and Hopf bifurcations by empty diamonds. (b) Two-dimensional phase diagram in the $(J_c, \bar{\eta})$ plane showing the saddle node curves (LLP) as black solid curves and the transverse Hopf (TH) boundary as yellow solid line. The dashed lines refer to transverse instabilities connecting unstable solutions, which are therefore not observable in the system evolution. Other parameters for this figure: $\tau_s = 2$, $\Delta = 0.5$, $J_s = 20$, and $\alpha = 0$.

(2) region V: below the upper saddle-node curve the asymmetric solution characterized by antiphase oscillations is still stable and coexists with the low-activity fixed point. The lower branch of the saddle-node curve to the right of the zero-Hopf point delimits the region where spontaneous symmetry breaking occurs. The dashed yellow curve in region V is the continuation of the Hopf point reported in Fig. 6(a) for $J_c = 40$, which leads to unstable oscillations of asymmetric nature (unstable TH curve).

C. Two coupled populations with SFA

We now investigate the collective dynamics emerging in a system of two symmetrically coupled neural masses with spike-frequency adaptation. We first analyze two coupled inhibitory populations and then two coupled excitatory ones.

1. Two inhibitory populations

Let us first analyze the phase diagram in the $(J_c, \bar{\eta})$ plane for two coupled inhibitory populations with SFA. This is shown in Fig. 7(a) and it is quite similar to the one obtained in the absence of SFA in Fig. 5(a). In particular, we observe the same four dynamical regions I–IV previously reported for the case in the absence of adaptation. However, due to SFA, we have a new transverse Hopf (TH) line [yellow curve in Fig. 7(a)], which originates from a Bogdanov Takens (BT) bifurcation point. This new instability leads to the emergence of slow collective oscillations in antiphase in region VI. An example of this collective dynamics is reported in Fig. 7(c). By crossing the longitudinal Hopf (LH) instability curve [blue

solid line in Fig. 7(a)], the slow and fast oscillations, associated to the LH, combine themselves in region V, giving rise to the so-called nested oscillations. In each population these COs are characterized by a slowly varying envelope joined to fast oscillations. These oscillations resemble the so-called θ-nested γ oscillations observable in various part of the brain, where the slow modulation is in the θ-range and the fast oscillations in the γ band. In particular, these have been measured in the hippocampus of behaving rats and shown to be relevant for cognitive tasks, including navigation, sensory association, and working memory [29–31,54]. In the present case, due to the symmetry breaking, the two populations reveal slow-fast nested oscillations in antiphase as shown in Fig. 7(b).

We then proceed to investigate the role played by the adaptation parameter α on the collective dynamics. Therefore, we computed the bifurcation diagram in the $(\bar{\eta}, \alpha)$ plane, as shown in Fig. 8. Let us first focus on the supercritical longitudinal Hopf (LH) instability (blue solid line), which divides regions I and III, where we find symmetric fixed points and fast symmetric COs, respectively. Here, even for extremely large α values, COs are observable. This seems in contradiction with the analysis reported for the single inhibitory population with SFA. In such a case, for a constant value of $\bar{\eta}$, the increase of the α parameter led to a shrink of the region where COs were observable, until they disappear completely for sufficiently large α values. However, in the present case, we see that the inhibitory effect, due to the adaptation, can be compensated by increasing the neuron excitability $\bar{\eta}$. Indeed, the positive slope of the LH curve is consistent with this interpretation.
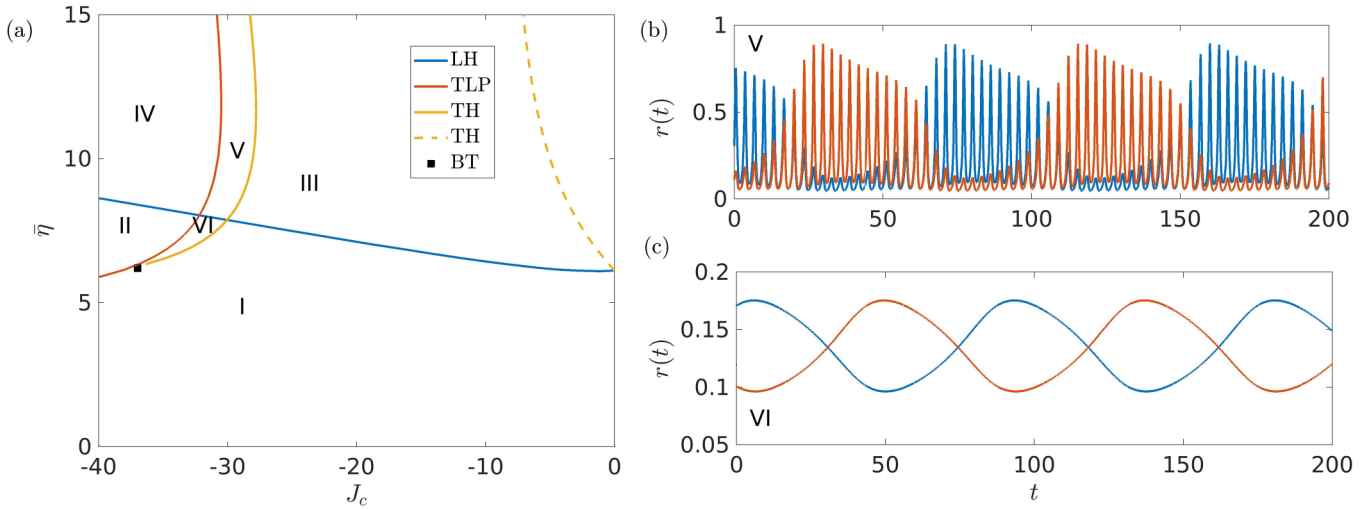
FIG. 7. Two symmetrically coupled inhibitory populations with SFA (a) Phase diagram in the $(J_c, \bar{\eta})$ plane depicting the longitudinal (transverse) stability boundary with red (blue) lines. Stability boundaries of stable (unstable) solutions are shown as solid (dashed) lines. Longitudinal and transverse bifurcation curves divide the parameter space in six relevant regions. (b) Typical dynamical evolution in region V: slow-fast nested collective oscillations in antiphase in the two populations for $(J_c, \bar{\eta}) = (-32, 10)$. (c) Typical dynamical evolution in region VI: antiphase collective oscillations emerging for $(J_c, \bar{\eta}) = (-32, 7.5)$. The values of the other parameters are $\tau_s = 2$, $\Delta = 0.5$, $J_s = -20$, and $\alpha = 5$.

For low α values we find a transverse instability curve corresponding to a bifurcation line of limit points (TLP) (red solid curve), which separates symmetric fixed points in region I from asymmetric fixed points in region II. By increasing $\bar{\eta}$ we encounter the longitudinal Hopf bifurcation line (LH) previously described, where the asymmetric fixed
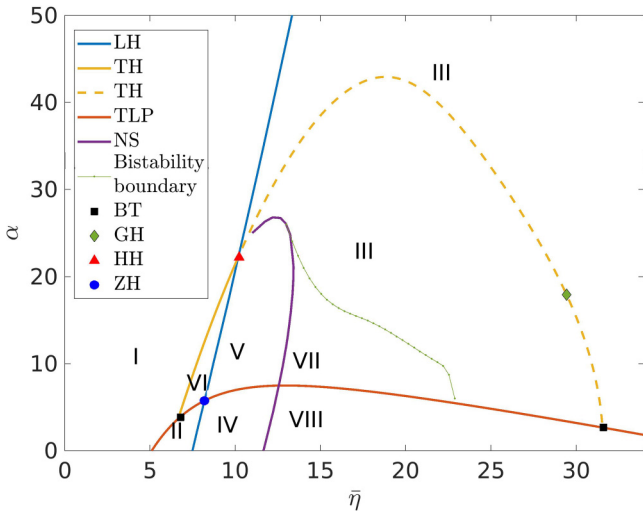

FIG. 8. Two symmetrically coupled inhibitory populations with SFA. Phase diagram in the $(\bar{\eta}, \alpha)$ plane showing eight regions with different dynamical regimes which are listed in details in Table I. Regions I–VI as in Fig. 7; region VII: Coexistence between fast symmetric COs and slow-fast nested COs; region VIII: coexistence between fast symmetric and asymmetric COs. The symbols refer to codimenstion two bifurcation points: namely, Bodgnatov-Takens (BT) (black square), generalized-Hopf (GH) (green diamond), Hopf-Hopf (HH) (red triangle), and zero-Hopf (ZH) (blue circle). The remaining parameters are fixed as $J_c = -33$, $J_s = -20$, $\Delta = 0.5$, $\tau_A = 10$, and $\tau_s = 2$.

points bifurcate toward asymmetric fast COs in region IV. By following the TLP curve we observe, at a Bogdanov-Takens (BT) point located at $(\bar{\eta}, \alpha) \approx (6.8, 3.8)$, the emergence of a transverse Hopf (TH) bifurcation line (yellow solid curve in Fig. 8). This TH line ends at another Bogdanov-Takens (BT) point observable at very large $\bar{\eta}$ values, always along the TLP curve. The symmetry breaking associated to the transverse Hopf instability leads from stable symmetric fixed points in region I to slow COs in antiphase in region VI. By following the TLP curve, we encounter a zero-Hopf (ZH) codimension two bifurcation point, when this meets the LH line. The LH line separates region VI, displaying slow COs in antiphase, from region V where slow-fast nested COs in antiphase are observable.

In this phase diagram we can identify two new dynamical regimes with respect to the ones reported in Fig. 7(a), both characterized by the coexistence of different stable solutions. Firstly, let us observe that symmetric fast COs emerge only to the right of the Neimark-Sacker (NS) curve [55] (in violet in the figure), that emerges in the proximity of a Hopf-Hopf (HH) codimension two bifurcation point (red triangle) [56]. Indeed, we have found coexisting regimes between symmetric and asymmetric oscillations only to the right of the NS curve. These regimes exist in region VII, where we have found stable fast symmetric COs together with stable slow-fast nested COs, and in region VIII, where stable fast symmetric and asymmetric COs coexist. The green dotted line in Fig. 8, separating region VII and III, where only symmetric solutions persist, has been determined by direct simulations of the coupled neural masses.

The last codimension two bifurcation point can be observed along the unstable transverse Hopf branch (yellow dashed line), corresponding to a generalized Hopf (GH) (green diamond). It distinguishes between a supercritical Hopf bifurcation line at higher $\bar{\eta}$ values and a subcritical one at lower $\bar{\eta}$. However, since it involves unstable

TABLE I. Two symmetrically coupled inhibitory populations with SFA. Macroscopic dynamical regimes observable in the different regions identified in Fig. 8. While regions I–IV are already present in the system without SFA, regions V–VIII are observable only when introducing SFA in the system.

Two coupled inhibitory populations	
Region	Dynamical Regime
I	Symmetric fixed points
II	Asymmetric fixed points
III	Fast symmetric COs
IV	Fast asymmetric COs
V	Slow-fast nested COs in antiphase
VI	Slow COs in antiphase
VII	Coexistence between fast symmetric COs and slow-fast nested COs in antiphase
VIII	Coexistence between fast symmetric and asymmetric COs

solutions, these are not observable in the dynamics of the system.

The scenario that we have described in the $(\bar{\eta}, \alpha)$ parameter space is summarized in Table I.

2. Two excitatory populations

Let us now consider two symmetrically coupled excitatory populations with SFA. For not too large α values we observe the same scenario as the one reported in Fig. 6(b) in the absence of adaptation. Therefore, we do not describe in detail the possible solutions here, since they have been already reported in the previous Sec. III B 2. To observe new dynamical regimes due to adaptation, we rather consider the $(\bar{\eta}, \alpha)$ plane for sufficiently large α values. Indeed, as shown in Fig. 9(a), a new region VI emerges where identical bursting oscillations can be observed in both populations, as shown in

Fig. 9(b). This region is delimited by two LH lines separating it from region I, where the fixed point, corresponding to low firing activity, is stable, and region IV, where fast COs in antiphase are observable. The low-activity state gets unstable by crossing the almost vertical LH line; once crossed the LH line, it gives rise to symmetric relaxation oscillations corresponding to a burst characterized by a silent regime connected to fast modulated oscillations. This bursting dynamics is analogous to the one reported for a single excitatory population with SFA, shown in Fig. 2(b). The other LH line determines the stability of the COs in antiphase, which emerge via a transverse Hopf (TH) bifurcation (red solid line) from the destabilization of the high-activity fixed point present in region III.

As observable in Fig. 9(a), for low α values and high negative $\bar{\eta}$ values, the system shows only two possible stable regimes separated by a longitudinal saddle node bifurcation curve (black solid line): a low-activity fixed point in region I and a coexistence between two fixed points with different activity levels in region II. Further increasing $\alpha, \bar{\eta}$ along the branch point curve (LLP) leads to a codimension two ZH point. Here emerges a new longitudinal Hopf curve (blue solid line) which delimits the region V, where a coexistence between antiphase COs and a low-activity fixed point is present. As we have already shown, antiphase COs are present also in region IV, as the unique stable solution. Beyond these broken symmetry solutions, where the same attractor is visited at different times by the two populations, we have been able to identify another solution with broken symmetry at quite large α values, as shown in Fig. 9(c). In this case, both populations display bursting activity, characterized by the same period of the slow modulation, but with different amplitudes and frequencies for the modulated fast spiking oscillations.

An overview of the possible dynamical regimes emerging in a system of two symmetrically coupled excitatory populations is reported in Table II.
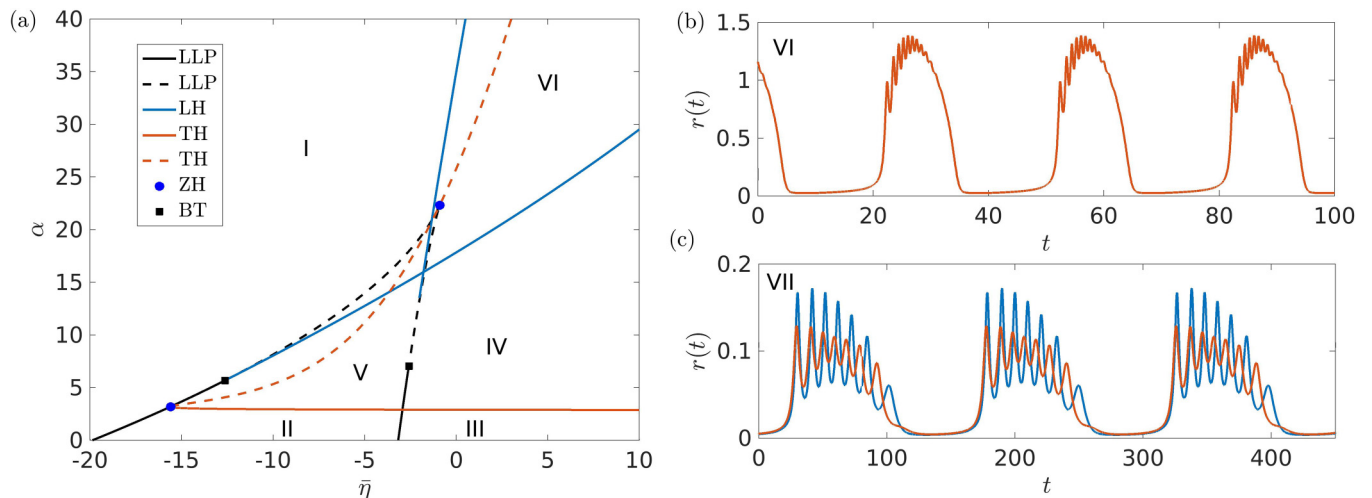

FIG. 9. Two symmetrically coupled excitatory populations with SFA. (a) Phase diagram in the $(\bar{\eta}, \alpha)$ space showing six regions with different dynamics. Parameters for this diagram: $J_c = 20$, $J_s = 8$, $\Delta = 0.5$, $\tau_A = 10$ and $\tau_s = 2$. Regions I–V as in Fig. 6(b). (b) Region VI: symmetric bursting dynamics $(\bar{\eta}, \alpha) = (5, 30)$. (c) An example of bursting with broken symmetry for parameters $(\bar{\eta}, \alpha) = (23, 70)$. The regimes here shown are summarized in Table II.

TABLE II. Two symmetrically coupled excitatory populations with SFA. Macroscopic dynamical regimes observable in the different regions identified in Fig. 9. While regions I–V are already present in the system without SFA, regions VI–VII are observable only when introducing SFA in the system.

Two coupled excitatory populations	
Region	Dynamical Regime
I	Low-activity symmetric fixed points
II	Asymmetric fixed points (one low-activity and one high-activity fixed point)
III	High-activity symmetric fixed points
IV	Fast asymmetric (antiphase) COs
V	Coexistence between fast COs in antiphase and low-activity fixed points
VI	Symmetric bursting activity
VII	Asymmetric bursting activity

IV. θ-γ CROSS-FREQUENCY COUPLING DUE TO ADAPTATION

In this section we will focus on the dynamical regimes where cross-frequency couplings among slow and fast collective oscillations are observable for two coupled excitatory or inhibitory populations with SFA. In particular, due to their relevance for brain dynamics we will consider as slow rhythms the ones in the θ range (1–12 Hz) and as fast ones COs in the γ band (30–130 Hz).

A. θ-nested γ oscillations in coupled inhibitory populations with SFA

For two coupled inhibitory populations with SFA the slow-fast nested COs in antiphase shown in Fig. 7(b) can be classified as instances of CFCs. Here we will consider parameters allowing the slow (fast) rhythms to be in the θ (γ) range and we will analyze the dependence of these rhythms on the adaptation. In this case the phase of the θ modulation affects the amplitude of the γ-oscillations: this CFC mechanism is termed phase amplitude coupling and it turns out to have been observed in several parts of the brain [35]. Since the time traces of the two populations are identical, but in antiphase, we limit the analysis to only one trace. As shown in Fig. 10(a), one observes distinct oscillatory periods: a slow intercycle period T_s, which identifies the time in between two successive θ oscillations, and a fast intracycle period T_f between successive γ peaks.

The evaluation of the power spectral density $S(f)$ for the time trace reported in Fig. 10(a) reveals a single peak at low frequencies $f_s \simeq 5$ Hz [see Fig. 10(b)] and a main peak at high frequencies, located around $f_f \simeq 35$ Hz, plus smaller peaks in correspondence of the combinations of the two main frequencies $f_f \pm k f_s$ with $k = 1, 2, 3, \ldots$ [as shown in Fig. 10(c)].

It is of particular interest to understand how the parameter α, measuring the strength of the adaptation, influences these two frequencies. The analysis is reported in Fig. 10(d) and 10(e) for the chosen set of parameters and for $\alpha \in [20, 100]$. It is evident that f_f, that identifies the main peak in the power spectrum of the fast signal component, decreases monotonously for increasing α, while the main peak of the
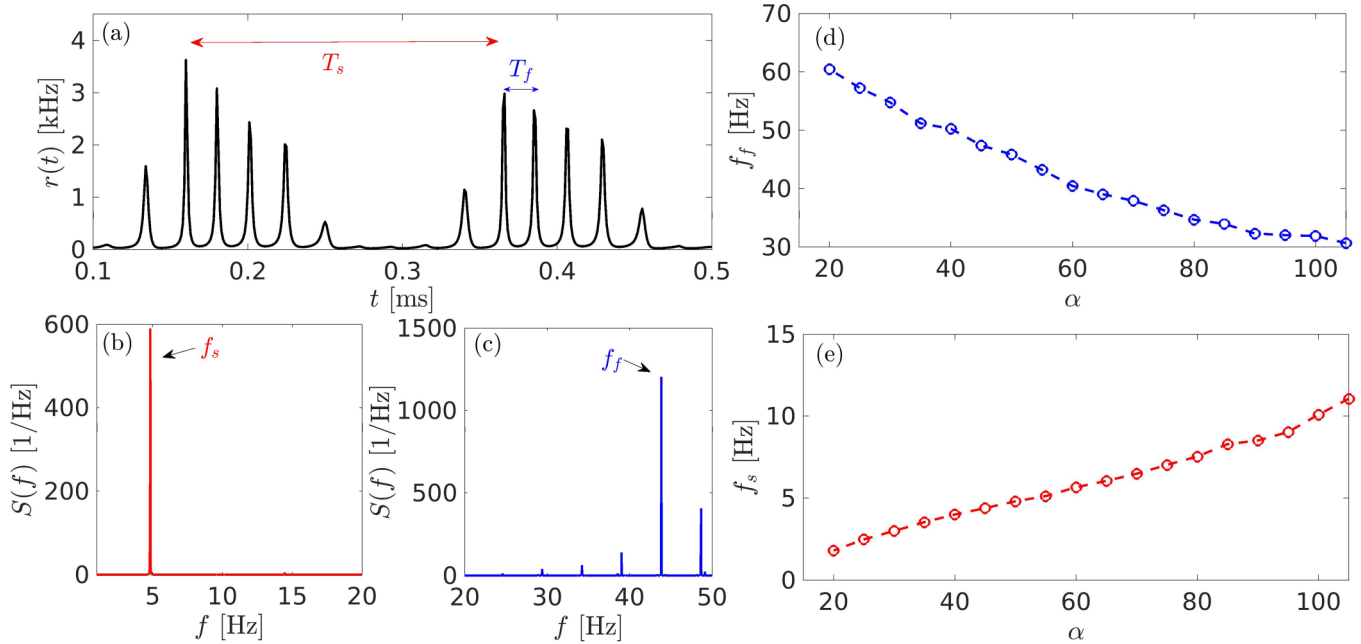

FIG. 10. Two coupled inhibitory populations with SFA. (a) Time trace of the firing rate $r(t)$ for one of the two populations. The other population shows the same evolution, but shifted in phase. The two relevant periods of the oscillatory behavior are reported as T_s (slow) and T_f (fast). (b) Power spectral density $S(f)$ of the time trace filtered using a third-order Butterworth low pass filter with cut-off frequency of 15 Hz. (c) Same as in panel (b) using a third-order Butterworth high pass filter with cut-off frequency of 20 Hz. (d), (e) Variation of the fast-and slow-frequency components f_f and f_s, respectively, as a function of the adaptation parameter α. Parameters used here: $\bar{\eta} = 28$, $J_s = -20$, $J_c = -47$, $\Delta = 0.5$, $\tau_S = 20$ ms, and $\tau_A = 100$ ms. For panels (a)–(c), a value of $\alpha = 50$ was chosen.
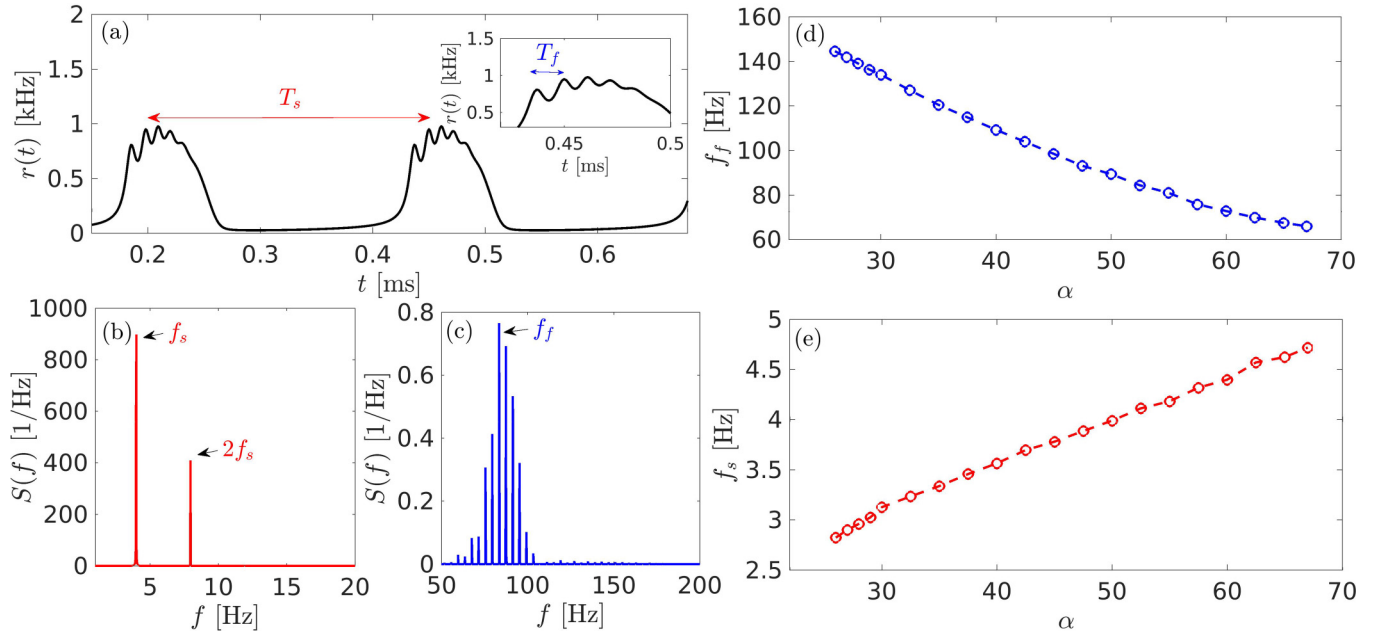
FIG. 11. Two coupled excitatory populations with SFA. (a) Time trace of the firing rate $r(t)$ for one of the two populations. The other population shows exactly the same evolution. The two relevant periods of the oscillatory behavior are sketched as T_s (slow) and T_f (fast) (for this see the enlargement in the inset). (b) Power spectral density $S(f)$ of a filtered time trace obtained by using a third-order Butterworth with cut-off frequency of 10 Hz. (c) Same as in panel (b) by using a third-order Butterworth high pass filter with cut-off frequency of 80 Hz. (d), (e) Variation of the fast- and slow-frequency components f_f and f_s, respectively, as a function of the adaptation constant α. Parameters used here: $\bar{\eta} = 5$, $J_{in} = 8$, $J_{ex} = 20$, $\Delta = 0.5$, $\tau_S = 20$ ms, and $\tau_A = 100$ ms. For panels (a)–(c), a value of $\alpha = 50$ was chosen.

slow signal component f_s increases. In particular, f_s grows from 2 to 11 Hz, while the fast peak f_f decreases from 60 to 30 Hz, thus exploring the whole range of the so-called slow γ rhythms observable in the hippocampus [30].

B. θ-γ population bursts in coupled excitatory populations with SFA

For coupled excitatory neural masses with SFA it is possible to observe CFC in the form of a burst connecting a resting state to a fast spiking activity. In this case the dynamics is the same for both populations. For specific choices of the parameters the interburst period is in the θ-range, while the intrabursts are γ oscillations [an example is reported in Fig. 11(a)]. Analogously to the previous subsection, we can define T_s as the interburst period, while T_f represents the intraburst period, as shown in Fig. 11(a). By performing low-pass (high-pass) filtering of the time signal reported in the above-mentioned figure (i.e., the firing rate $r(t)$ of one of the two populations), we can detect the main peak $f_s \simeq 4$ Hz ($f_f \simeq 80$ Hz) for the slow (fast) component of the power spectrum $S(f)$; see Figs. 11(c) and 11(d). At variance with the previous case, the phase of the θ rhythm does not modulate only the amplitude of the γ-oscillations, but also their periods (frequencies), therefore the spectrum reported in Fig. 11(c) reveals that an entire band of frequencies between 70 and 100 Hz is indeed excited.

Also in the present case, we analyze the dependence of f_s and f_f on the adaptation parameter α. By varying α in the range [25,68], we observe that f_s (f_f) increases (decreases) for growing values of α as before. However, while the variation of f_s is quite limited from 2.8 to 4.8 Hz, the γ peak f_f ranges

from 130 to 60 Hz, i.e., f_f is now exploring the fast γ range [30].

V. DISCUSSION

In this paper we have analyzed the influence of the spike-frequency adaptation mechanism on the macroscopic dynamics of single as well as symmetrically coupled neural populations connected via either excitatory or inhibitory exponentially decaying post-synaptic potentials. The macroscopic dynamics has been investigated in terms of next-generation neural masses reproducing exactly the dynamics of fully coupled networks of quadratic integrate-and fire spiking neurons in the thermodynamic limit. This low-dimensional mean-field reduction has allowed for the estimation of the corresponding bifurcation diagrams. In particular, we mostly focused on the instabilities of the stationary states with emphasis on the longitudinal and transverse nature of the instabilities in symmetrically coupled populations.

In a single population with a fixed distribution of the neural excitabilities, SFA favors the emergence of population bursts when the coupling is excitatory, while it hinders the emergence of periodic population spikes in inhibitory networks. This is related to the fact that SFA acts as an effective inhibition with a slow timescale τ_a. In inhibitory networks in the absence of adaptation, oscillations are already present, controlled by the fast synaptic timescale τ_s. Therefore, in this case, SFA leads to an additional inhibitory effect that can eventually kill the population spiking for sufficiently large amplitude of the adaptation parameter [7,22]. However, in excitatory networks COs are absent without adaptation, while

these are promoted by the SFA, which represents the only source of inhibition. As we have shown by performing a slow-fast decomposition, the population burst evolves on a timescale controlled by τ_a connecting a low firing state to a high firing one, that is approached via fast damped population spikes characterized by a fast timescale of the order of τ_s.

The coupling of two identical populations in a symmetric way leads to the emergence of collective solutions with broken symmetry for cross-couplings larger than self-couplings ($|J_c| > |J_s|$). These solutions can be classified as chimera-like for the inhibitory case and antiphase population spikes in the excitatory one. The chimera-like solutions correspond to asymmetric fixed points and fast COs. These kind of solutions have been usually identified whenever the self-coupling was larger than the cross-coupling in identically coupled populations of phase oscillators [57] and excitatory neurons [41,52]. In all these cases the action of the phase oscillators (neurons) on their own population was more effective in promoting the synchronized (firing) activity than that of the oscillators (neurons) belonging to the other population. This scenario would emerge for two inhibitory coupled populations whenever $|J_c| > |J_s|$. Therefore, consistently with our analysis, we can affirm to have reported, for the first time to our knowledge, chimera-like states in purely inhibitory neural systems.

Chimera-like states have been reported also in Ref. [41] for two coupled next-generation neural masses interacting via steps of currents for the excitatory and inhibitory case. However, it should be noticed that in Ref. [41], the inhibitory case refers to a situation where the self-coupling is excitatory, while the cross-coupling is inhibitory. This choice violates the Dale's principle [58] that states that neurons can transmit either excitatory or inhibitory post-synaptic signals, but not both at the same time. However, a setup like the one proposed in Ref. [41], could be shown to mathematically represent two excitatory populations coupled to an inhibitory pool [59], thus resulting in a setup involving at least three neural populations, which is definitely different from the one we have examined.

The addition of SFA leads to new macroscopic solutions and regimes besides the ones observed in the absence of adaptation. In the inhibitory case, new collective solutions with broken symmetry are observable, that correspond to slow collective oscillations and slow-fast nested oscillations, both occurring in antiphase in the two populations. Furthermore, the fast symmetric COs can coexist with fast asymmetric ones as well as with slow-fast nested COs in antiphase. The new solutions observable for excitatory populations with SFA correspond to population bursts that can be either symmetric or asymmetric. A summary of all the observable regimes is reported in Tables I and II.

The evolution of two symmetrically coupled neural masses with SFA can lead to interesting CFC phenomena, where oscillations induced by the fast synaptic timescale and by the slow adaptation are present at the same time and interact among them. In particular, we have examined macroscopic solutions exhibiting cross-frequency coupling in the θ-γ range and the dependence of the fast f_f and slow f_s frequencies on the adaptation, both for the inhibitory and excitatory case.

As a first result, we observe that the reduction of SFA leads to an increase in the frequency of the θ rhythm, joined to a decrease in the γ frequencies. This is analogous to the effect of cholinergic modulation, as shown in several experiments based on EEG recordings of the hippocampus and the olfactory cortex [60,61]. In particular, cholinergic modulation induces an increase in the number of γ oscillations, joined to a decrease in the frequency of the θ rhythm [25–27]. Indeed, consistently with these results, it has been shown that cholinergic drugs are responsible for a reduction of SFA in pyramidal cells [24].

Furthermore, it has been shown that θ-γ CFC is favored by the presence of the cholinergic neurotransmitters [38,39] and, therefore, by a reduction of SFA [62]. This is somehow consistent with our results, since we have shown that the ratio f_f/f_s decreases for increasing α, thus determining a reduction of the number of γ oscillation events inside a single θ cycle for higher adaptation values. Therefore, according to the hypothesis that the neural code for multi-item messages is organized by θ-γ nested brain oscillations [36,63], we expect that, for large adaptation values, the number of coded items will diminish, thus reducing the neural coding effectiveness.

Finally, we have shown that, in our model, θ rhythm can modulate either slow or fast γ oscillations, analogously to those identified in the hippocampus and other brain areas [33]. In particular, we observe that, in presence of SFA, slow γ are associated to inhibitory dynamics, while excitatory populations support fast γ oscillations.

As far as the generality of our results is concerned, since the QIF neuron represents the normal form of Hodgkin class I excitable membranes, we can expect that our findings will extend to all this class of neurons. Furthermore, spiking and bursting regimes have been previously identified in a single population of (leaky) integrate and fire (LIF) neurons with SFA [23,40], thus suggesting that the regimes here identified will probably emerge also for symmetrically coupled populations of LIF neurons. By following the recent advances in the development of next-generation neural mass models, we plan in the future to further extend the analysis here presented to QIF networks including more biologically realistic aspects, such as the delays in the synaptic transmissions [64] or the sparseness in the synaptic connections [65].

Finally, our analysis could be useful to develop new models of Central Pattern Generators, which are responsible for the generation of rhythmic movements, since these models are often based on two interacting oscillatory populations with adaptation, as reported for the spinal cord [66] and the respiratory system [67]. Finally, the model of the medullary circuitry reported in Ref. [68] can be taken as a cue for a further interesting application of coupled neural masses with SFA, like the modelization of rhythmic whisking in rodents and, in particular, the entrainment of whisking by breathing.

APPENDIX: STABILITY OF THE STATIONARY SOLUTIONS FOR A SINGLE POPULATION

Here we show the steps to calculate the stability boundaries for the stationary solutions of the single population. We start by using the adimensional system defined in Eq. (9). The characteristic polynomial evaluated at the equilibrium (r_0, v_0, s_0, a_0) is given by

$$p(\lambda) = \frac{2\alpha r_0 \Lambda_s + \Lambda_a\{-2Jr_0 + [4\pi^2 r_0^2 + (\lambda - 2v_0)^2]\Lambda_s\}}{\tau_a \tau_s},$$

$$(A1)$$

with $\Lambda_a = (1 + \lambda\tau_a)$ and $\Lambda_s = (1 + \lambda\tau_s)$. In general, a bifurcation occurs when one or more eigenvalues cross the imaginary axis, namely whenever $\lambda = i\omega$, hence we look for solutions of the form $p(i\omega) = 0$. Replacing λ with $i\omega$ in Eq. (A1) and equating to zero leads to

$$2\alpha r_0 \Omega_s + \Omega_a\{-2Jr_0 + [4\pi^2 r_0^2 + (2v_0 - i\omega)^2]\Omega_s\} = 0,$$

$$(A2)$$

with $\Omega_s = (1 + i\omega\tau_s)$ and $\Omega_a = (1 + i\omega\tau_a)$. For Eq. (A2) to be satisfied, both imaginary and real parts of $p(i\omega)$ should be zero, namely:

$$\text{Re}[p(i\omega)] = 0; \quad \text{Im}[p(i\omega)] = 0. \quad (A3)$$

By solving $\text{Re}[p(i\omega)] = 0$ ($\text{Im}[p(i\omega)] = 0$) in Eq. (A3) we get the solutions ω_{Re}^* (ω_{Im}^*). These have the form

$$\omega_{\text{Re}}^* = \pm\frac{\sqrt{P_1 \pm \sqrt{P_2 + P_1^2}}}{\sqrt{2\tau_a \tau_s}}, \quad (A4a)$$

$$\omega_{\text{Im}}^* = \pm\sqrt{2P_3}, \quad \omega_{\text{Im}}^* = 0, \quad (A4b)$$

with

$$P_1 = 1 + 4\pi^2 r_0^2 \tau_a \tau_s + 4v_0^2 \tau_a \tau_s - 4v_0(\tau_a + \tau_s), \quad (A5a)$$

$$P_2 = 8[Jr_0 - 2r_0^2 - r_0(2\pi^2 r_0 + \bar{\alpha})]\tau_a \tau_s, \quad (A5b)$$

$$P_3 = \frac{2r_0 - 2r_0^2(\tau_a + \tau_s) - r_0[-J\tau_a + \alpha\tau_s + 2\pi^2 r_0(\tau_a + \tau_s)]}{-\tau_s + \tau_a(-1 + 4v_0\tau_s)}.$$

$$(A5c)$$

Recalling that $v_0 = -\Delta/(2\pi r_0)$, all the expressions are parametrized by the coordinate r_0 of the equilibrium. Equating (A4a) and the nonzero solutions of Eq. (A4b), and solving for one of the parameters, it is possible to parametrize the Hopf bifurcation solution via r_0. Similarly, equating (A4a) with the trivial solution $\omega_{\text{Im}}^* = 0$, the limit point-type bifurcations (saddle-node, pitchfork, and transcritical) can be obtained.

[1] H. R. Wilson and J. D. Cowan, Kybernetik **13**, 55 (1973).
[2] M. Mattia and P. Del Giudice, Phys. Rev. E **66**, 051917 (2002).
[3] E. S. Schaffer, S. Ostojic, and L. F. Abbott, PLoS Comput. Biol. **9**, e1003301 (2013).
[4] E. Montbrió, D. Pazó, and A. Roxin, Phys. Rev. X **5**, 021028 (2015).
[5] A. Byrne, M. J. Brookes, and S. Coombes, J. Comput. Neurosci. **43**, 143 (2017).
[6] Á. Byrne, R. D. O'Dea, M. Forrester, J. Ross, and S. Coombes, J. Neurophysiol. **123**, 726 (2020).
[7] A. Ceni, S. Olmi, A. Torcini, and D. Angulo-Garcia, Chaos **30**, 053121 (2020).
[8] H. Bi, M. Segneri, M. di Volo, and A. Torcini, Phys. Rev. Res. **2**, 013042 (2020).
[9] H. Taher, A. Torcini, and S. Olmi, PLoS Comput. Biol. **16**, e1008533 (2020).
[10] M. Segneri, H. Bi, S. Olmi, and A. Torcini, Front. Comput. Neurosci. **14**, 47 (2020).
[11] R. Gast, H. Schmidt, and T. R. Knösche, Neural Comput. **32**, 1615 (2020).
[12] M. Gerster, H. Taher, A. Škoch, J. Hlinka, M. Guye, F. Bartolomei, V. Jirsa, A. Zakharova, and S. Olmi, Front. Syst. Neurosci. **15**, 675272 (2021).
[13] R. Gast, T. R. Knösche, and H. Schmidt, Phys. Rev. E **104**, 044310 (2021).
[14] P. Varona, J. Ibarz, L. López-Aguado, and O. Herreras, J. Neurophysiol. **83**, 2192 (2000).
[15] L. M. de la Prida, G. Huberfeld, I. Cohen, and R. Miles, Neuron **49**, 131 (2006).
[16] E. M. Izhikevich, Int. J. Bifurcat. Chaos **10**, 1171 (2000).

[17] C. van Vreeswijk, Phys. Rev. E **54**, 5522 (1996).
[18] S. Olmi, R. Livi, A. Politi, and A. Torcini, Phys. Rev. E **81**, 046119 (2010).
[19] M. A. Whittington, R. D. Traub, and J. G. Jefferys, Nature (London) **373**, 612 (1995).
[20] C. Van Vreeswijk, L. Abbott, and G. Bard Ermentrout, J. Comput. Neurosci. **1**, 313 (1994).
[21] N. Brunel and V. Hakim, Neural Comput. **11**, 1621 (1999).
[22] F. Devalle, A. Roxin, and E. Montbrió, PLoS Comput. Biol. **13**, e1005881 (2017).
[23] C. v. Vreeswijk and D. Hansel, Neural Comput. **13**, 959 (2001).
[24] S. P. Aiken, B. J. Lampe, P. A. Murphy, and B. S. Brown, Br. J. Pharmacol. **115**, 1163 (1995).
[25] R. D. Traub, R. Miles, and G. Buzsáki, J. Physiol. **451**, 653 (1992).
[26] E. Barkai, R. E. Bergman, G. Horwitz, and M. E. Hasselmo, J. Neurophysiol. **72**, 659 (1994).
[27] S. M. Crook, G. B. Ermentrout, and J. M. Bower, Neural Comput. **10**, 837 (1998).
[28] G. Buzsaki, *Rhythms of the Brain* (Oxford University Press, Oxford, UK, 2006).
[29] G. Buzsáki and X.-J. Wang, Annu. Rev. Neurosci. **35**, 203 (2012).
[30] L. L. Colgin, T. Denninger, M. Fyhn, T. Hafting, T. Bonnevie, O. Jensen, M.-B. Moser, and E. I. Moser, Nature (London) **462**, 353 (2009).
[31] M. A. Belluscio, K. Mizuseki, R. Schmidt, R. Kempter, and G. Buzsáki, J. Neurosci. **32**, 423 (2012).
[32] H. Zhang and J. Jacobs, J. Neurosci. **35**, 12477 (2015).

[33] L. L. Colgin, Nat. Rev. Neurosci. **17**, 239 (2016).

[34] A. Sirota, S. Montgomery, S. Fujisawa, Y. Isomura, M. Zugaro, and G. Buzsáki, Neuron **60**, 683 (2008).

[35] R. T. Canolty and R. T. Knight, Trends Cognit. Sci. **14**, 506 (2010).

[36] J. E. Lisman and O. Jensen, Neuron **77**, 1002 (2013).

[37] J. L. Butler, P. R. Mendonça, H. P. Robinson, and O. Paulsen, J. Neurosci. **36**, 4155 (2016).

[38] E. L. Newman, S. N. Gillet, J. R. Climer, and M. E. Hasselmo, J. Neurosci. **33**, 19635 (2013).

[39] W. M. Howe, H. J. Gritton, N. A. Lusk, E. A. Roberts, V. L. Hetrick, J. D. Berke, and M. Sarter, J. Neurosci. **37**, 3215 (2017).

[40] G. Gigante, M. Mattia, and P. Del Giudice, Phys. Rev. Lett. **98**, 148101 (2007).

[41] I. Ratas and K. Pyragas, Phys. Rev. E **96**, 042212 (2017).

[42] G. B. Ermentrout and N. Kopell, SIAM J. Appl. Math. **46**, 233 (1986).

[43] H. Taher, Ph.D. thesis, Université Côte d'Azur, 2021.

[44] E. Ott and T. M. Antonsen, Chaos **18**, 037113 (2008).

[45] T. B. Luke, E. Barreto, and P. So, Neural Comput. **25**, 3207 (2013).

[46] S. Coombes and Á. Byrne, in *Nonlinear Dynamics in Computational Neuroscience* (Springer, Berlin, 2019), pp. 1–16.

[47] A. S. Pikovsky and P. Grassberger, J. Phys. A: Math. Gen. **24**, 4587 (1991).

[48] S. Olmi, Chaos **25**, 123125 (2015).

[49] A. Dhooge, W. Govaerts, and Y. A. Kuznetsov, ACM Trans. Math. Softw. **29**, 141 (2003).

[50] J. Guckenheimer and Y. A. Kuznetsov, Scholarpedia **2**, 1854 (2007).

[51] L. Chen and S. A. Campbell, J. Comput. Neurosci. **50**, 445 (2022).

[52] S. Olmi, A. Politi, and A. Torcini, Europhys. Lett. **92**, 60007 (2011).

[53] Y. Kuramoto, in *Chemical Oscillations, Waves, and Turbulence* (Springer, Berlin, 1984), pp. 111–140.

[54] G. Buzsáki, C. H. Vanderwolf *et al.*, Brain Res. Rev. **6**, 139 (1983).

[55] Y. A. Kuznetsov and R. J. Sacker, Scholarpedia **3**, 1845 (2008).

[56] J. Guckenheimer and Y. A. Kuznetsov, Scholarpedia **3**, 1856 (2008).

[57] D. M. Abrams and S. H. Strogatz, Phys. Rev. Lett. **93**, 174102 (2004).

[58] H. Dale, Br. Med. J. **2**, 1161 (1934).

[59] K.-F. Wong and X.-J. Wang, J. Neurosci. **26**, 1314 (2006).

[60] J. Konopacki, M. B. MacIver, B. H. Bland, and S. H. Roth, Brain Res. **405**, 196 (1987).

[61] M. Biedenbach, Exp. Neurol. **16**, 464 (1966).

[62] Y. Yang, H. Gritton, M. Sarter, S. J. Aton, V. Booth, and M. Zochowski, PLoS Comput. Biol. **17**, e1009235 (2021).

[63] J. Lisman and G. Buzsáki, Schiz. Bull. **34**, 974 (2008).

[64] F. Devalle, E. Montbrió, and D. Pazó, Phys. Rev. E **98**, 042214 (2018).

[65] D. S. Goldobin, M. di Volo, and A. Torcini, Phys. Rev. Lett. **127**, 038301 (2021).

[66] H. Lindén and R. W. Berg, Front. Hum. Neurosci. **15**, 719388 (2021).

[67] J. E. Rubin, B. J. Bacak, Y. I. Molkov, N. A. Shevtsova, J. C. Smith, and I. A. Rybak, J. Comput. Neurosci. **30**, 607 (2011).

[68] M. Deschênes, J. Takatoh, A. Kurnikova, J. D. Moore, M. Demers, M. Elbaz, T. Furuta, F. Wang, and D. Kleinfeld, Neuron **90**, 374 (2016).